Efficient Exciton Diffusion and Resonance-Energy Transfer in Multilayered Organic Epitaxial Nanofibers

Luciana Tavares,*,[†] Michele Cadelano,[‡] Francesco Quochi,[‡] Clemens Simbrunner,[§,⊥] Günther Schwabegger,[§] Michele Saba,[‡] Andrea Mura,[‡] Giovanni Bongiovanni,[‡] Demétrio Antônio da Silva Filho,[‖] Wiliam Ferreira da Cunha,[‖] Horst-Günter Rubahn,[†] and Jakob Kjelstrup-Hansen[†]

[†]NanoSYD, Mads Clausen Institute, University of Southern Denmark, Alsion 2, DK-6400 Sønderborg, Denmark
[‡]Department of Physics, University of Cagliari, Complesso Universitario di Monserrato, I-09042 Monserrato, Cagliari, Italy
[§]Institute of Semiconductor and Solid State Physics, Johannes Kepler University Linz, A-4040 Linz, Austria
[⊥]Institute of Solid State Physics, University of Bremen, D-28359 Bremen, Germany
[‖]Institute of Physics, University of Brasilia, 04455, DF 70919-970 Brasília, Brazil

Ⓢ Supporting Information

ABSTRACT: Multilayered epitaxial nanofibers are exemplary model systems for the study of exciton dynamics and lasing in organic materials because of their well-defined morphology, high luminescence efficiencies, and color tunability. We use temperature-dependent continuous wave and picosecond photoluminescence (PL) spectroscopy to quantify exciton diffusion and resonance-energy transfer (RET) processes in multilayered nanofibers consisting of alternating layers of para-hexaphenyl (p6P) and α-sexithiophene (6T) serving as exciton donor and acceptor material, respectively. The high probability for RET processes is confirmed by quantum chemical calculations. The activation energy for exciton diffusion in p6P is determined to be as low as 19 meV, proving p6P epitaxial layers also as a very suitable donor material system. The small activation energy for exciton diffusion of the p6P donor material, the inferred high p6P-to-6T resonance-energy-transfer efficiency, and the observed weak PL temperature dependence of the 6T acceptor material together result in an exceptionally high optical emission performance of this all-organic material system, thus making it well suited, for example, for organic light-emitting devices.
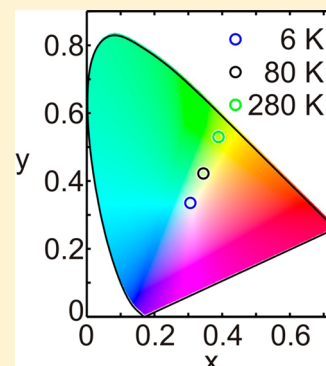
INTRODUCTION

Many studies have been devoted to organic semiconductors largely because of their significant application potential in optoelectronic devices that results from their useful intrinsic properties combined with low manufacturing costs. Strategies to improve the efficiency of organic light-emitting devices (OLEDs)[1−3] and organic solar cells (OSC)[4,5] have in particular been the focus of many recent reports. Exciton diffusion is one of the determining factors of OLED efficiency roll-off at high brightness;[6,7] it affects the device efficiency of OSCs[8,9] and also influences the bimolecular recombination losses and thereby lasing threshold in organic lasers.[10] Therefore, the understanding and quantification of exciton diffusion is fundamental for further improving organic device performance.

Organic π-conjugated small molecules can self-assemble on a template surface to form crystalline, needle-shaped nanofibers.[11,12] Such nanofibers can be prepared from a single material[11] or, as recent reports have demonstrated, as multilayered nanofibers composed of p6P and 6T[13,14] consisting of a relatively thick (∼0.1 μm) p6P nanofiber template onto which a periodic multilayer of 6T and p6P was deposited.[13] Furthermore, it has been demonstrated that such a

growth procedure can be applied to a broad class of molecules.[15] The initial p6P template layer was deposited on a muscovite mica substrate resulting in the formation of mutually parallel p6P nanofibers, which were aligned along the mirror symmetry directions of the mica surface.[11,16] The well-defined growth direction and morphology observed for p6P on mica (in contrast to organic nanofibers made from other materials or on other substrates[17−19]) makes this system a useful template for the subsequent periodic deposition of 6T and p6P layers.[13,14] The photoluminescence (PL) emission spectrum of the p6P/6T multilayered nanofiber samples can be tuned by varying the thickness of either the p6P or the 6T layers.[13,14] If ultrathin (monolayer thickness) 6T layers are used, it results in a homogeneous coverage of the p6P template fibers and a homogeneous green PL emission, as illustrated in Figure 1a.[13,14]

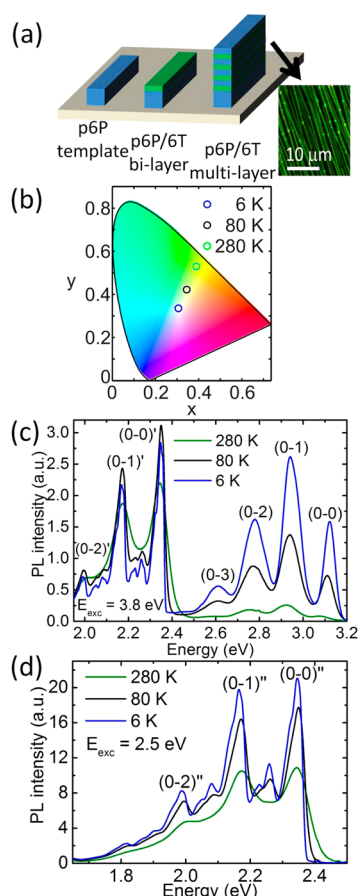Both single-layered (only p6P) and multilayered p6P/6T nanofibers show unique characteristics (for example, polarized

Figure 1. (a) Schematic representation of p6P and 6T nanofibers grown on muscovite mica and fluorescence microscope image (λ_{exc} = 365 nm) of sample 1. (b) CIE chromaticity diagram and (c) photoluminescence spectra obtained at different temperatures illuminating the sample with 3.8 eV photon energy, which directly excites fluorescence from the p6P layers, while the 6T layers emit light because of sensitization from the excited p6P. (d) Photoluminescence spectra of the 6T monolayer directly excited with 2.5 eV photon energy, which is below the optical band gap of p6P.

light emission[13,20]) due to their crystallinity and the specific orientation of the emitting dipoles along the molecules' long axes. Furthermore, the p6P nanofibers have a high PL quantum yield;[21] their PL spectrum shows a well-defined vibronic progression;[22] they can function as optical (both photonic[23] and plasmonic[24]) waveguides; and amplified spontaneous emission (ASE) and laser action can be achieved under femtosecond optical excitation.[11,25] Random lasing caused by light scattering from imperfections in the nanofiber morphology (which provides the optical feedback) has been observed in the deep blue for p6P nanofibers[25] and also in multilayered p6P/6T heteroepitaxial nanofibers, in which the wavelength of the nanofiber's lasing was tuned from deep blue to red-orange.[10] Lasing in the monomolecular regime for single-layered p6P nanofibers was achieved at a temperature of 80 K,[26] whereas the 6T (in the multilayered p6P/6T nanofibers) monomolecular lasing was achieved at room temperature, which is because the exciton diffusion and thus the bimolecular recombination in the p6P/6T heteroepitaxial nanofibers is much less effective in the 6T phases than in p6P.[10] In addition, the large spectral overlap between the donor emission and acceptor absorption enables efficient resonance-energy transfer

(RET) between the two materials.[13,14] A comparable material class is electrospun nanofibers from blend polymer materials that brings advantages such as mechanical flexibility, low fabrication costs, and ease of material doping.[27] However, the p6P/6T nanofibers form a monolithic, highly oriented heteroepitaxial system yielding highly polarized emission. The planar geometry can also bring additional advantages, e.g., realization of device structures via lamination with the possibility of integrating high power density LEDs for indirect electrical pumping.[28]

Because of the unique properties of the p6P/6T multilayered nanofibers, we have chosen this system for detailed investigations of the exciton dynamics and resonance-energy donor-to-acceptor transfer processes that determine the resulting optical properties. In this work, we study the efficiency of the exciton diffusion and energy-transfer processes in the multilayered nanofibers via low-temperature PL spectroscopy and quantify the contribution of the different recombination processes via time-resolved PL measurements. Theoretical calculations using density functional theory (DFT) and its time-dependent approach (TDDFT) were also carried out in order to obtain equilibrium energies, geometries, and frequencies for both ground (S_0) and first excited (S_1) states of p6P and 6T. These properties allow us to understand better the mechanisms behind the absorption and emission processes involved in the isolated molecules and to build a qualitative model to understand the energy transfer in the p6P/6T complex.

EXPERIMENTAL SECTION

Nanofiber Growth. Multilayered p6P/6T heteroepitaxial nanofibers were prepared on muscovite mica via hot wall epitaxy (HWE) under high-vacuum conditions.[13,14] Two samples were investigated via low-temperature PL and time-resolved studies. Sample 1 was deposited at a substrate temperature of 140 °C. After the deposition of the p6P template (nominal thickness of 84 nm), a sequence of 50 cycles of 6T monolayers (~0.26 nm) intercalated with p6P (~1.51 nm) were deposited. Sample 2 was deposited at a substrate temperature of 120 °C. After the deposition of the p6P template, a sequence of 10 cycles of 6T monolayers (~0.37 nm) intercalated with p6P (~16.3 nm) was deposited.

Temperature-Dependent PL Spectroscopy. The PL spectra at low temperature were obtained under vacuum conditions by controlling the sample temperature with a Helium cryo-cooler and recording the luminescence spectra with a spectrometer (Acton Research Co. SpectraPro-150) coupled to a cooled CCD array (Princeton Instrument PIXIS 100) while exciting the sample with either a He−Cd laser emitting at 325 nm (3.8 eV photon energy) or an Ar-ion laser (161 LGS, LG Laser Tech) emitting at 488 nm (2.5 eV photon energy).

Temperature-Dependent Time-Resolved Photoluminescence Spectroscopy. Samples were kept in a coldfinger cryostat (Janis Research Co. ST-500) fed with liquid N_2 for measurements in the 80−300 K temperature range and photoexcited by the frequency-doubled pulses (~100 fs duration, 375 nm wavelength) of a passively mode-locked Ti-Sapphire laser (Spectra Physics Tsunami) running at 82 MHz focused to a spot of ~100 μm in diameter. Optical absorption by the samples, strongly polarization dependent, was maximized using a half-wave plate placed in the laser beam. The photoluminescence emission was collected in the trans-

mission geometry by a lens system and acquired by a streak camera (Hamamatsu C5680) working synchronously with the exciting laser pulses coupled to a grating spectrometer (Acton Research Co. SpectraPro 2300i). Temporal resolution of the apparatus was approximately 10 ps.

DFT Calculations. Geometries, frontier orbitals, and total energies of the ground state (S_0) and first excited state (S_1) of p6P and 6T were obtained using DFT. We make use of two different DFT functionals: (i) the M06-2X functional,[29,30] which has proven to properly describe the spectroscopic properties of these type of systems,[30,31] and (ii) the CAM-B3YP functional, which has a good track record in the description of the electronic processes in organic molecules.[32,33] The 6-31G(d) basis set was used for all calculations presented here. This basis set was chosen because of the relative large size of the systems under investigation in addition to the successful reproduction of the absorption and emission data of short oligomers.[33,34] All simulations were carried out using the Gaussian09 program suite.[35]

■ RESULTS AND DISCUSSION

Temperature-Dependent PL Spectroscopy on Multi-layered Nanofibers. By photoexcitation of the p6P molecules with a photon energy above the 6T absorption spectrum, a spectrum that contains emission from both p6P and 6T can be observed.[13,14] The p6P emission is the directly excited PL, whereas the 6T emission results from sensitization of the 6T monolayer, via Förster resonance-energy transfer (FRET) from the excited p6P molecules due to the overlap of the emission spectrum of the p6P and the absorption spectrum of the 6T material.[10,13,14] Time-resolved measurements of the 6T emission have revealed that two distinct exciton populations within the p6P layers are involved in the sensitization process. Those generated within a distance corresponding to the Förster radius (3.6 nm in p6P)[14] from the p6P/6T interface are transferred on a very short time-scale via RET giving rise to prompt 6T emission, while the p6P excitons generated further away but within the diffusion range from the p6P/6T interface result in a delayed 6T emission via diffusion-assisted RET. To further understand the contributions of the short (Förster's) and long (diffusion-mediated) transfer, we investigated two samples with different number of layers and layer thickness using PL spectroscopy and ultrafast time-resolved measurements of the luminescence dynamics and their temperature dependence. Sample 1 consists of a p6P template with a thickness of 84 nm on top of which 50 cycles of ~0.26 nm 6T and ~1.51 nm p6P were deposited, while sample 2 was prepared by a sequence of 10 cycles of monolayer-thick 6T (~0.37 nm) intercalated with much thicker p6P layers (~16.3 nm).

Figure 1b shows the 1931 Commission Internationale de l'Eclairage (CIE) chromaticity diagram of the PL spectra from sample 1 acquired at different temperatures in vacuum and under illumination with ultraviolet (UV) light (3.8 eV photon energy). A change of sample temperature from 280 to 6 K causes the emission color to gradually change from green (CIE coordinates, x = 0.39, y = 0.54 at 280 K) to a more white/blue color (CIE coordinates, x = 0.31, y = 0.34 at 6 K). These changes are also reflected in the PL spectra shown in Figure 1c, in which both p6P and 6T emission can be observed simultaneously. The illumination with UV directly excites fluorescence from the p6P layers because of the radiative decay of singlet excitons[36] from the vibrational ground state of the

first excited electronic state to various vibrational levels of the electronic ground state. At room temperature, the characteristic peaks from p6P are positioned at 3.09 eV (0–0), 2.93 eV (0–1), 2.77 eV (0–2), and 2.61 eV (0–3),[22] while the peaks originating from the 6T monolayers are at 2.35 eV (0–0)′, 2.18 eV (0–1)′, and 2.01 eV (0–2)′.[13,37−39] Figure 1c shows that the p6P emission intensity increases by an order of magnitude when cooling the substrate from 280 to 6 K. This indicates that the nonradiative processes (related to exciton diffusion to quenching sites and to the p6P/6T interface) are suppressed at low temperature. These aspects will be discussed in detail in the section Modeling of the PL Temperature Dependence. In Figure 1c, one can also observe that the green emission intensity from the sensitized 6T monolayers increases when cooling from 280 to 80 K and then decreases again upon further cooling to 6 K. A weak temperature dependence is also observed by directly exciting the 6T monolayer with 2.5 eV photon energy, which is below the optical gap of p6P[40,41] and therefore excites only the 6T,[10] as shown in Figure 1d, where the spectra from the intrinsic decay process of the 6T excitons are collected at different temperatures. The weak temperature dependence of the directly excited PL from the 6T monolayer, consisting of thermal (homogeneous) broadening not involving significant intensity redistribution among the vibronic peaks, suggests that the nonradiative processes are not significant, i.e., that the 6T has intrinsic high quantum yield, confirming the appropriateness of 6T as the acceptor material for this system. We attribute this huge temperature dependence difference between p6P and 6T to the fact that crystalline p6P layers are H aggregates while the ultrathin 6T layers have a radically different aggregation state (most presumably weakly bound J aggregates).[38,39]

The intensities of the spectrally integrated p6P and 6T emissions are plotted in Figure 2a. The PL intensity of the p6P emission monotonically increases with decreasing temperature, and a qualitatively similar behavior is observed for the directly excited 6T; however, the directly excited 6T exhibits a much
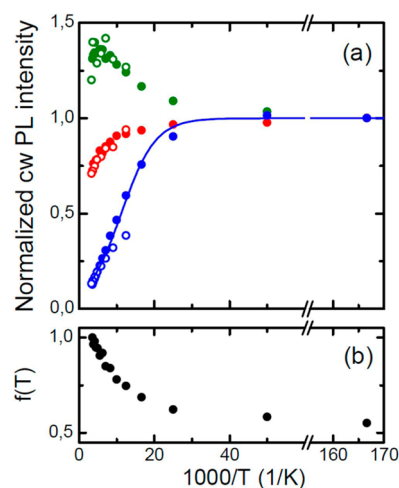

Figure 2. (a) Full dots: cw luminescence intensity of p6P (blue) and 6T (green) photoexcited at 3.8 eV; 6T (red) luminescence intensity under direct excitation at 2.5 eV. Blue continuous line is the fitting curve of the p6P luminescence intensity data (see text for details). Hollow dots: steady-state p6P and 6T emission intensities reconstructed from transient photoluminescence data. (b) Ratio between emission intensities of the sensitized and directly excited 6T measured under 3.8 and 2.5 eV pumping, respectively.

weaker temperature dependence. Compared to the p6P and the directly excited 6T emission, the PL intensity of the sensitized 6T follows a different trend, in which the intensity first increases with decreasing temperature, but then reaches a maximum and decreases again. We interpret this as being due to two processes with different temperature dependencies in the 6T emission process: the sensitization process (which depends on the exciton diffusion and energy transfer) and the actual intrinsic decay of the 6T excitons. We propose that the temperature dependence of the PL from the sensitized 6T can therefore be described as a product of a function $f(T)$, which describes the temperature dependence of the sensitization process, and a function $\eta_{PL,6T}$ that describes the intrinsic radiative decay yield, which is proportional to the temperature dependence of the directly excited 6T emission:

$$I(6T)_{sens} \propto f(T)\eta_{PL,6T} \propto f(T)I(6T)_{direct}$$

$$\therefore f(T) \propto \frac{I(6T)_{sens}}{I(6T)_{direct}} \qquad (1)$$

An elementary rate equation model for the p6P and 6T excited-state populations predicts that

$$\frac{I(6T)_{sens}}{I(6T)_{direct}} = \frac{W_{p6P}}{W_{6T}}\eta_{sens} \qquad (2)$$

where η_{sens} is the 6T emission sensitization quantum yield and W_{6T} and W_{p6P} are the pump absorption rates for direct 6T and p6P excitation, respectively. The rate equation model for the exciton densities is provided in the Supporting Information. It is clear that if the p6P and 6T optical absorption does not depend on temperature, the function $f(T)$ gives the temperature dependence for the 6T emission sensitization process (η_{sens}). The temperature dependence of the normalized ratio of the intensities of the sensitized and directly excited 6T (function $f(T)$) is shown in Figure 2b. This ratio decreases when decreasing the temperature from 280 to 6 K presumably because of less efficient exciton diffusion and therefore less efficient energy transfer from p6P to the 6T at lower temperatures.

Theoretical Calculations. To better understand the fundamental processes involved in the photoemission of p6P molecules and subsequent absorption of 6T, a DFT investigation of the ground state (S_0) and first excited state (S_1) of p6P and 6T was carried out. As the first step, we discuss the ground state (S_0) equilibrium geometries. The optimized ground state of isolated p6P and 6T shows the typical alternating twists of the rings. (The definition of the dihedral angles and their values are presented in Figure S1 and Table S1 in the Supporting Information). The average dihedral angle between the rings computed with M06-2X [CAM-B3LYP] was found to be 37° [38°] for p6P and 20° [22°] for 6T.

Upon excitation, as expected, both molecules tend to assume a more planar structure. The excited state of 6T becomes planar with both functionals, whereas for p6P, the average dihedral angle reduces to 22° [21°] when the M06-2X [CAM-B3LYP] was used.

Figure 3a shows the ground-state (S_0) highest occupied molecular orbital (HOMO) and lowest unoccupied molecular orbitals (LUMO) wavefuction for both p6P and 6T, whereas Figure 3b shows the frontier orbital energies of the two oligomers, computed using CAM-B3LYP. In solid state, both p6P[42] and 6T[43] are observed to be linear and planar molecules,
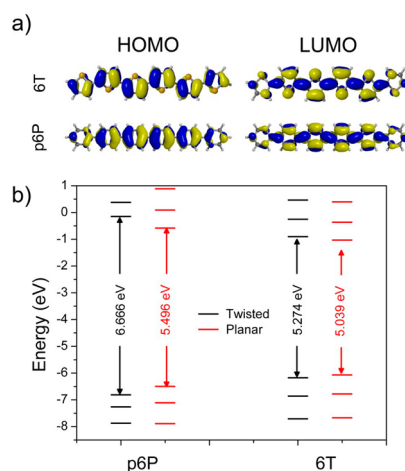

Figure 3. (a) 6T (top) and p6P (bottom) ground-state HOMO (left) and LUMO (right) wave functions. (b) CAM-B3LYP ground state (S_0) frontier orbital energies and HOMO−LUMO gap for p6P (left) and 6T (right). Both fully optimized (twisted) and optimized under the planarity constraint (planar) are presented.

in both ground and excited states. Thus, to better compare the experimental results with our calculations, we also optimized p6P and 6T subjected to the constraint of being planar and evaluated the impact of this constraint in the $S_0 \rightarrow S_1$ transition energy, which is also included in Figure 3b. The impact of planarization on p6P is larger than that on 6T, as expected from the larger deviation from planarity presented by the former oligomer. A comparison between the HOMO−LUMO gap of the two planar structures shows that p6P has still a larger gap compared to that of 6T, but the difference between the two has reduced from 1.39 eV in the twisted form to 0.46 eV in the planar (solid-state-like) form. The results for M06-2X shows a similar trend (see Figure S2 in the Supporting Information); however, the mismatches between the gap of p6P and 6T were computed to be 1.37 and 0.837 eV, respectively.

This small difference (on the order of tenths of electron-volts) in the HOMO−LUMO gap and the fact that p6P has a larger gap compared to 6T already suggests that p6P can absorb a higher-energy photon and transfer this energy to 6T, as was observed for other thiophene-based systems.[44]

To further investigate the mechanisms behind the energy transfer between the two molecules in the ground state (S_0) and first excited state (S_1), the corresponding potential energy surfaces (PESs) were analyzed. Four important energies were extracted from time-dependent density functional theory calculations. These energies are (i) the optimized ground-state energy $(E_{S_0 S_0})$, (ii) the first excited-state energy with the ground-state optimized geometry $(E_{S_1 S_0})$, (iii) the ground-state energy with the optimized S_1 geometry $(E_{S_0 S_1})$, and (iv) the optimized first excited-state energy $(E_{S_1 S_1})$. No symmetry constraints were used in these geometry optimizations. These four energies allow us to compare not only the vertical energy gaps but also the amount of energy that can be lost in geometrical relaxation after a vertical transition.

Figure 4 shows these energies for 6T and p6P calculated using CAM-B3LYP (see results for M06-2X in Figure S3 in the Supporting Information). The optical gap is represented by the vertical transition between the ground state and the first excited state, i.e., the energy difference $(E_{S_1 S_0} - E_{S_0 S_0})$. The two energy
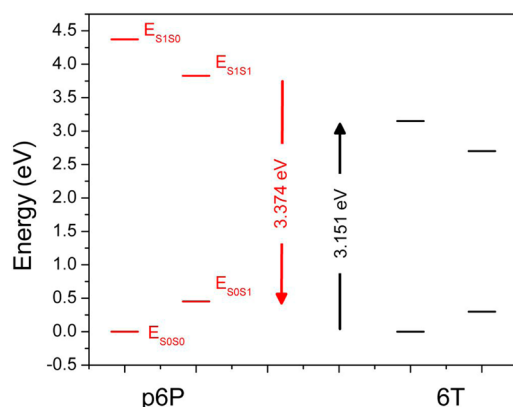
Figure 4. S_0 and S_1 potential energy levels for (left) p6P and (right) 6T using CAM-B3LYP. (Center) p6P $S_1 \rightarrow S_0$ transition energy from its lowest vibronic state (red) together with the 6T $S_0 \rightarrow S_1$ transition from its lowest vibronic state (black).

differences, $E_{S_1S_0} - E_{S_1S_1}$ and $E_{S_0S_1} - E_{S_0S_0}$ are the excited-state and the ground-state relaxation energies, respectively. Here it is important to highlight that both p6P and 6T assume a quinoid-like (and thus planar) conformation in the first excited state.[45] As a result, the relaxation energy associated with the geometry relaxation after a vertical transition from the ground state to the excited state $(S_0 \rightarrow S_1)$ is larger than the related energy associated with the inverse process (i.e., the $S_1 \rightarrow S_0$ relaxation).[46] Figure 4 allows for direct comparison between the experimental results reported here for the vertical transition from the vibrational ground state of the first excited electronic state $(E_{S_1S_1})$ to the ground state $(E_{S_0S_1})$ and our theoretical calculations. The experimental value of 3.09 eV for p6P [2.35 eV for 6T] compares well with the corresponding theoretical values of 3.37 eV [2.40 eV] obtained with CAM-B3LYP and 3.37 eV [2.42 eV] obtained with M06-2X, respectively.

To have a resonance-energy transfer between the emission of p6P and the absorption of 6T, one must have a match between the energy emitted by p6P and the energy absorbed by 6T. Using CAM-B3LYP [M06-2X], we computed these energies, i.e., the energy required for a transition from the S_1 lowest vibrational state to S_0 for p6P and the energy required for a transition from the S_0 lowest vibrational state to the S_1 state for 6T, and obtained 3.374 and 3.151 eV [3.374 and 3.123 eV], respectively. The difference of only 0.2 eV (for both functionals) validates our assumption that a resonance-energy transfer is happening.

To further characterize this energy transfer, a simulation of the vibronic resolved absorption spectrum of 6T together with the counterpart emission spectrum of p6P must be carried out.

A direct calculation of the complete absorption and emission spectra using Gaussian09 was attempted, as was done before for fused oligothiophenes.[44] However, the overlap between the two vibrational ground states of S_0 and S_1 is negligibly small, thus suggesting that this approach is not appropriate to treat p6P and 6T molecules. This fact was recently observed by Lumpi et al.[31] and is attributed to the considerable changes in geometry when going from the ground to the excited states in these systems (the planarization mentioned before). These changes restrict the validity of the Franck–Condon approach used by Gaussian09 to generate vibronically resolved spectra.

A detailed study of the potential energy surfaces of the ground and excited states of 6T and p6P and subsequent generation of the vibrationally resolved spectra is beyond the scope of this manuscript and will be presented elsewhere.

Exciton Dynamics in Multilayered Sample. To further elucidate the exciton dynamics and explain the temperature dependence of the PL spectra (Figure 1c) we have used temperature-dependent, ultrafast time-resolved PL spectroscopy that can provide quantitative data on the exciton diffusion and energy-transfer processes. The excitons, which are generated in p6P within a distance from the p6P/6T interface corresponding to the Förster radius, are transferred via direct RET on a very short time scale (faster than 20 ps, the time resolution of our experimental setup). On the other hand, p6P excitations generated further away from the interface, but still in the exciton diffusion length region, are transferred in a two-step process: (i) excitons first diffuse to the interface and (ii) excitons are transferred via RET (diffusion-assisted RET). This occurs on a time scale that is accessible with our experimental setup. The results shown here for the time-resolved measurements were obtained for sample 2, which has thicker p6P layers compared to sample 1. Samples with p6P layer thicknesses larger than the Förster radius allow the observation of both direct and diffusion-assisted RET of p6P excitations to 6T. On the other hand, time-resolved data are difficult to analyze in samples with very thin p6P layers (thickness less than the Förster radius) because in this case a very large fraction of the p6P excitons are involved in 6T sensitization only through direct RET (mostly unresolved in the p6P decay dynamics), whereas diffusion-assisted RET is practically absent.

Figure 5 shows the time-resolved, temperature-dependent measurements obtained from 300 K down to 80 K. The luminescence decay was obtained using a streak camera that provides both temporally and spectrally resolved data. This allows separate analysis of the temporal behavior of the two parts of the spectra corresponding to p6P emission and 6T
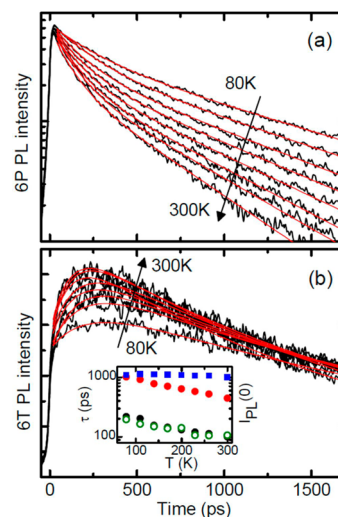

Figure 5. Time-resolved PL obtained from sample 2 at different temperatures for (a) the p6P emission intensity integrated over the interval 400−480 nm and (b) the 6T emission intensity integrated in the range of 510−650 nm. Red continuous lines are best fits based on a biexponential decay function (a) and an exponential activation–decay function (b) as described in the text. The inset of panel (b) shows the temperature dependence of the p6P decay time constants, τ_1 and τ_2 (black and red dots, respectively), of the 6T activation time constant (hollow green dots) and of the initial p6P luminescence intensity, $I_{PL}(t = 0)$) (blue squares) (see text for details).

emission. Figure 5a shows the time-resolved p6P emission intensity obtained by spectral integration over the 400−480 nm wavelength interval. In relaxation time approximation, the p6P dynamics is fitted with a biexponential decay curve as

$$I_{p6P}(t) = A_1 e^{-t/\tau_1} + A_2 e^{-t/\tau_2} \tag{3}$$

where the fast component (A_1, τ_1) represents the p6P exciton population involved in diffusion-assisted RET (generated within a distance from the p6P/6T interface corresponding to the diffusion length). The slow component (A_2, τ_2) represents the intrinsic decay in p6P and is attributed to the p6P excitons that do not reach the p6P/6T interface and therefore are unable to contribute to the 6T sensitization. The fast decaying PL component associated with the p6P excitons generated within the Förster distance from the p6P/6T interfaces is not visible because of the limited temporal resolution of the experiment, which is supposed to attenuate its amplitude to values not detectable on top of the (A_1, τ_1) and (A_2, τ_2) decaying components. Analysis of the fitting parameters can provide information on the temperature dependence of these processes. The temperature dependence of the decay time constants (τ_1 and τ_2) and the prompt PL emission intensity, which is estimated as the sum of the amplitudes of the two exponentials ($A_1 + A_2$), is plotted in the inset of Figure 5b. The time constant τ_1 is almost an order of magnitude smaller than τ_2, which suggests that diffusion-mediated RET is a highly efficient process in our all-organic heterostructures. Because the two time constants (τ_1 and τ_2) display the same temperature dependence, we also infer that not only p6P-to-6T long-range RET but also all other nonradiative p6P exciton recombination processes are mediated by exciton diffusion. Moreover, the initial p6P emission intensity exhibits very little variation in the 80−300 K temperature range, demonstrating that p6P optical absorption at the UV pump wavelength is temperature-insensitive. Figure 5b shows the sensitized 6T emission intensity spectrally integrated over the wavelength interval between 510 and 650 nm. The 6T dynamics is fitted as[14]

$$I_{6T}(t) = A_p e^{-t/\tau_d} + A_{act}(1 - \exp(t/\tau_d - t/\tau_{act}))e^{-t/\tau_d} \tag{4}$$

where the single exponential decay (A_p, τ_d) describes the prompt emission from 6T excitons generated through direct RET (from p6P excitons originating within the Förster radius). The second, delayed term stems from p6P excitons that diffuse to transfer energy, where the 6T dynamics are fitted with an exponential activation (τ_{act}, activation time) and decay curve (A_{act}, τ_{act}, τ_d) depicting the evolution of the 6T excitons generated through diffusion-assisted RET. The inset in Figure 5b also shows that the 6T activation time (τ_{act}) data nicely overlap with the fast p6P decay (τ_1), further confirming that 6T delayed emission is activated by p6P excitations through RET. We note that diffusion-assisted RET has been treated in relaxation-time approximation with a single time constant. From a theoretical point of view, this represents a simplification of the exciton diffusion kinetics; however, it is consistent with the experimental data. The donor exponential decay component with the shorter decay time perfectly matches the evolution of the acceptor delayed emission, which is very well fitted using a single exponential rise function (inset of Figure 5b). Moreover, a detailed account of the kinetics of diffusion-

assisted RET[47] and related data analysis[48] is beyond the scope of this paper.

Modeling of the PL Temperature Dependence. The conclusion from the time-resolved results in the inset in Figure 5b enables us to model the temperature dependence of the PL spectra (Figure 1c). The fluorescence intensity (I_{p6P}) is proportional to the quantum yield (η_{PL}), which can be described by

$$I_{p6P} \propto \eta_{p6P,PL} = \frac{\frac{1}{\tau_R}}{\frac{1}{\tau_R} + \frac{1}{\tau_{NR}}} = \frac{1}{1 + \frac{\tau_R}{\tau_{NR}}} \approx \frac{\tau_{NR}}{\tau_R}(\tau_R \gg \tau_{NR}) \tag{5}$$

where τ_R is the radiative decay time constant and τ_{NR} is the (total) nonradiative decay time constant.[49] As proposed by Wen et al.[50] we will also assume that the exciton diffusion (and thus nonradiative p6P exciton recombination) can be described as a temperature-activated process

$$\tau_{diff} = \tau_0 e^{E_{diff}/kT} \tag{6}$$

where τ_{diff} is a characteristic time for exciton diffusion in p6P and E_{diff} is the activation energy, k is Boltzmann's constant and T is the temperature. From this we get the expression for the temperature dependence of the PL intensity:

$$\frac{I}{I_0} = \frac{1}{1 + \frac{\tau_R}{\tau_0}e^{-E_{diff}/kT}} \tag{7}$$

from which we can find the activation energy for the exciton diffusion process by fitting the p6P spectrally integrated PL intensities versus reciprocal temperature as shown in Figure 2a together with a fit to eq 7. The measured PL intensity of the p6P emission fits well to eq 7, from which we can extract E_{diff} ~19 meV. The small value of activation energy for exciton diffusion makes p6P very suitable as donor material in a multilayered organic epitaxial system. In crystalline rubrene, an activation energy of ~30 meV has been observed,[50] while significantly higher activation energies have been observed in disordered films, e.g., around 69 meV in an anthradithiophene derivative,[51] i.e., higher than the room-temperature thermal energy.

Temperature Dependence of the Intrinsic Emission from p6P and 6T. Steady-state PL intensities measured under continuous wave (cw) optical excitation can be estimated on the basis of the fit parameters of the excited-state dynamics retrieved from transient PL measurements. The amplitude A_1 is proportional to the population of photogenerated p6P excitons contributing to 6T sensitization through diffusion-assisted RET, whereas the amplitude A_2 scales as the population of those p6P excitons that recombine before reaching a p6P/6T interface. The exciton population involved in direct RET within the Förster distance from an interface can in turn be estimated to be proportional to $A_1(A_p/A_{act})$. The temperature dependence of the steady-state intensities reached under cw excitation can thus be calculated as

$$I(p6P) \propto A_1\tau_1 + A_2\tau_2 \tag{8}$$

$$I(6T)_{sens} \propto A_1\eta_{sens,diff}\tau_d + A_1(A_p/A_{act})\tau_d \tag{9}$$

$$I(6T)_{direct} \propto \tau_d \tag{10}$$

where $\eta_{sens,diff} = \tau_2/(\tau_{sens,diff} + \tau_2)$ is the diffusion-assisted 6T sensitization yield ($1/\tau_1 = 1/\tau_{sens,diff} + 1/\tau_2$). In eq 10 it is

further assumed that the absorbed pump power under 6T direct excitation, W_{6T}, is temperature-independent. Temperature trends based on eqs 8−10 are reported in Figure 2a as hollow dots. They nicely agree with the measured steady-state intensities in cw excitation experiments, confirming the overall consistency of the experimental data and the validity of the interpretation model of the PL intensity dynamics. Note that because the PL intensity with direct 6T excitation actually scales as τ_d, the above assumption of 6T photoabsorption as a temperature-insensitive quantity turns out to be valid, at least in the 80−300 K temperature range. It can be concluded that the function $f(T)$ introduced above represents the correct temperature trend of the 6T emission sensitization efficiency.

Temperature Dependence of the Quantum Yield of the Energy Transfer from p6P to 6T. Time-resolved PL measurements also enable the extraction of the quantum yield of the energy-transfer process from p6P to 6T. The total 6T energy sensitization quantum yield ($\eta_{sens,u}$) that includes the contributions from both the direct and diffusion-assisted RET processes can now be found as the following weighted average

$$\eta_{sens,u} = \frac{A_1 \eta_{sens,diff} + A_1 \frac{A_p}{A_{act}}}{A_1 + A_1 \frac{A_p}{A_{act}} + A_2} \tag{11}$$

where the contribution from the diffusion-assisted RET is the product of its weight (A_1) and its efficiency ($\eta_{sens,diff}$). The efficiency of direct RET (with weight $A_1(A_p/A_{act})$) is supposed to be unity (as it is an ultrafast process). Finally, the p6P exciton population that does not reach the interface (with weight A_2) has zero probability of generating an exciton in 6T ($\eta = 0$). The value $\eta_{sens,u}$ can be considered an upper bound on the efficiency of 6T emission sensitization through RET. The lower bound, $\eta_{sens,l}$, can be found by including only the diffusion-assisted RET term

$$\eta_{sens,l} = \frac{A_1}{A_1 + A_2} \eta_{sens,diff} \tag{12}$$

In this approximation, the single exponential decay component (A_p, τ_d) of the 6T dynamics is traced back to direct photoexcitation of 6T and direct RET processes are fully neglected.

Upper and lower bounds for 6T sensitization quantum yield are displayed in Figure 6, where the function $f(T)$, extracted from cw measurements, is also shown with suitable normalization to match the lowest bound for η_{sens}. The sensitization efficiency depends on the p6P layer thickness. For samples with very thin p6P layers, whose thickness is comparable to or smaller than the exciton diffusion length in p6P, $\eta_{sens,u}$ is almost unity because all excitons are generated close to the interface and the sensitization process is therefore highly efficient, while for samples with thicker p6P layers, more p6P excitons decay without being transferred to 6T. The good agreement between the temperature trend of η_{sens} retrieved from the analysis of transient PL data and the one extracted from cw PL measurements further corroborates our understanding of the function $f(T)$ as the temperature dependence of the efficiency of 6T sensitization through the RET processes.

CONCLUSION

We have probed the energy-transfer and exciton recombination characteristics in multilayered epitaxial p6P/6T nanofibers by temperature-dependent PL spectroscopy using either 3.8 or 2.5
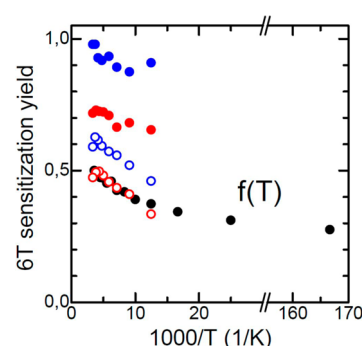

Figure 6. 6T emission sensitization quantum yields estimated on the basis of transient photoluminescence data versus reciprocal temperature; blue and red symbols refer to sample 1 and 2, respectively. Hollow dots: yield lower bounds. Full dots: yield upper bounds. Black full dots: ratio between cw emission intensities of the sensitized and directly excited 6T (function $f(T)$).

eV photons for stimulating the p6P or 6T layers, respectively. While the p6P quantum yield decreases by an order of magnitude between 6 and 300 K, the emission of the 6T monolayers exhibits much weaker temperature dependence, which was also observed under direct excitation of the 6T monolayers. To further elucidate the exciton dynamics, we have used temperature-dependent, ultrafast time-resolved PL spectroscopy to provide quantitative data on the exciton diffusion and energy-transfer processes. On the basis of this, we modeled the PL temperature dependence, which enabled us to extract the activation energy for exciton diffusion in crystalline p6P, which is only about 19 meV. The strong temperature dependence of the p6P PL emission was found to be due to a temperature-activated exciton diffusion process that results in a significant rise in PL quantum yield with decreasing temperature (an order of magnitude from 300 to 6 K). The 6T monolayers have a much weaker temperature dependence (40% increase from 300 to 6 K), presumably because of a different aggregation state. However, the sensitization process (diffusion-assisted RET from p6P) has a temperature dependence that counteracts the increase in intrinsic quantum yield at lower temperatures, giving rise to a 6T PL emission that initially increases by a few percent upon cooling from room temperature; however, the emission then starts to drop below ∼160 K, reaching around 0.8 of its room-temperature value at 6 K.

Theoretical calculations in the framework of density functional theory were used to characterize the potential energy surfaces of the ground (S_0) and first excited (S_1) states of p6P and 6T. By a comparison between the energy gap related to the emission of p6P and the absorption of 6T from their lowest vibronic state, we determined a mismatch of 0.2 eV of the order of the vibrational relaxation energy of the molecules, resulting in a high probability for resonance-energy transfer between the two molecules. This improved understanding of the exciton diffusion and resonance-energy-transfer processes in organic epitaxial heterostructures can aid in the development of new organic nanomaterials with desired optical properties.

ASSOCIATED CONTENT

Ⓢ Supporting Information

Rate equation model for p6P/6T exciton densities and DFT results of molecular geometries, orbital energies, and potential

energy levels. The Supporting Information is available free of charge on the ACS Publications website at DOI: 10.1021/acs.jpcc.5b02405.

■ AUTHOR INFORMATION

Corresponding Author
*E-mail: tavares@mci.sdu.dk. Phone: +45 6550 1645.

Notes
The authors declare no competing financial interest.

■ REFERENCES

(1) Reineke, S.; Lindner, F.; Schwartz, G.; Seidler, N.; Walzer, K.; Lüssem, B.; Leo, K. White Organic Light-Emitting Diodes with Fluorescent Tube Efficiency. *Nature* **2009**, *459*, 234−238.

(2) Nakanotani, H.; Higuchi, T.; Furukawa, T.; Masui, K.; Morimoto, K.; Numata, M.; Tanaka, H.; Sagara, Y.; Yasuda, T.; Adachi, C. High-Efficiency Organic Light-Emitting Diodes with Fluorescent Emitters. *Nat. Commun.* **2014**, *5*, 1−7.

(3) Capelli, R.; Toffanin, S.; Generali, G.; Usta, H.; Facchetti, A.; Muccini, M. Organic Light-Emitting Transistors with an Efficiency That Outperforms the Equivalent Light-Emitting Diodes. *Nat. Mater.* **2010**, *9*, 496−503.

(4) Scharber, M. C.; Sariciftci, N. S. Efficiency of Bulk-Heterojunction Organic Solar Cells. *Prog. Polym. Sci.* **2013**, *38*, 1929−1940.

(5) 12% efficiency in opaque and 7% efficiency in transparent organic solar cells. http://www.heliatek.com (accessed June 1, 2015).

(6) Hofmann, S.; Rosenow, T. C.; Gather, M. C.; Lüssem, B.; Leo, K. Singlet Exciton Diffusion Length in Organic Light-Emitting Diodes. *Phys. Rev. B: Condens. Matter Mater. Phys.* **2012**, *85*, 245209(1−8).

(7) Wünsche, J.; Reineke, S.; Lüssem, B.; Leo, K. Measurement of Triplet Exciton Diffusion in Organic Light-Emitting Diodes. *Phys. Rev. B: Condens. Matter Mater. Phys.* **2010**, *81*, 245201(1−11).

(8) Feron, K.; Belcher, W. J.; Fell, C. J.; Dastoor, P. C. Organic Solar Cells: Understanding the Role of Förster Resonance Energy Transfer. *Int. J. Mol. Sci.* **2012**, *13*, 17019−17047.

(9) Kozub, D. R.; Vakhshouri, K.; Kesava, S. V.; Wang, C.; Hexemer, A.; Gomez, E. D. Direct Measurements of Exciton Diffusion Length Limitations on Organic Solar Cell Performance. *Chem. Commun. (Cambridge, U.K.)* **2012**, *48*, 5859−5861.

(10) Quochi, F.; Schwabegger, G.; Simbrunner, C.; Floris, F.; Saba, M.; Mura, A.; Sitter, H.; Bongiovanni, G. Organic Nanofibers: Extending the Lasing Wavelength Coverage of Organic Semiconductor Nanofibers by Periodic Organic-Organic Heteroepitaxy. *Adv. Opt. Mater.* **2013**, *1*, 117−122.

(11) Kjelstrup-Hansen, J.; Simbrunner, C.; Rubahn, H.-G. Organic Surface-Grown Nanowires for Functional Devices. *Rep. Prog. Phys.* **2013**, *76*, 126502(1−24).

(12) Resel, R. Crystallographic Studies on Hexaphenyl Thin Films - A Review. *Thin Solid Films* **2003**, *433*, 1−11.

(13) Simbrunner, C.; Quochi, F.; Hernandez-Sosa, G.; Oehzelt, M.; Resel, R.; Hesser, G.; Arndt, M.; Saba, M.; Mura, A.; Bongiovanni, G.; et al. Organic-Organic Heteroepitaxy of Red-, Green-, and Blue-Emitting Nanofibers. *ACS Nano* **2010**, *4*, 6244−6250.

(14) Simbrunner, C.; Hernandez-Sosa, G.; Quochi, F.; Schwabegger, G.; Botta, C.; Oehzelt, M.; Salzmann, I.; Djuric, T.; Neuhold, A.; Resel, R.; et al. Color Tuning of Nanofibers by Periodic Organic-Organic Hetero-Epitaxy. *ACS Nano* **2012**, *6*, 4629−4638.

(15) Simbrunner, C.; Schwabegger, G.; Resel, R.; Dingemans, T.; Quochi, F.; Saba, M.; Mura, A.; Bongiovanni, G.; Sitter, H. Heteroepitaxy of Organic Nanofibers: Example of Ternaphthalene on *p*-Hexaphenyl. *Cryst. Growth Des.* **2014**, *14*, 5719−5728.

(16) Simbrunner, C.; Nabok, D.; Hernandez-Sosa, G.; Oehzelt, M.; Djuric, T.; Resel, R.; Romaner, L.; Puschnig, P.; Ambrosch-Draxl, C.; Salzmann, I.; et al. Epitaxy of Rodlike Organic Molecules on Sheet Silicates—A Growth Model Based on Experiments and Simulations. *J. Am. Chem. Soc.* **2011**, *133*, 3056−3062.

(17) Simbrunner, C.; Schwabegger, G.; Resel, R.; Dingemans, T.; Sitter, H. The Epitaxial Growth of Self-Assembled Ternaphthalene Fibers on Muscovite Mica. *Cryst. Growth Des.* **2014**, *14*, 442−449.

(18) Balzer, F.; Schiek, M.; Osadnik, A.; Wallmann, I.; Parisi, J.; Rubahn, H.-G.; Lützen, A. Substrate Steered Crystallization of Naphthyl End-Capped Oligothiophenes into Nanofibers: The Influence of Methoxy-Functionalization. *Phys. Chem. Chem. Phys.* **2014**, *16*, 5747−5754.

(19) Balzer, F.; Schiek, M.; Lützen, A.; Rubann, H. G. Self-Organized Growth of Organic Thiophene-Phenylene Nanowires on Silicate Surfaces. *Chem. Mater.* **2009**, *21*, 4759−4767.

(20) Schiek, M.; Balzer, F.; Al-Shamery, K.; Brewer, J. R.; Lützen, A.; Rubahn, H. G. Organic Molecular Nanotechnology. *Small* **2008**, *4*, 176−181.

(21) Quochi, F.; Andreev, A.; Cordella, F.; Orrù, R.; Mura, A.; Bongiovanni, G.; Hoppe, H.; Sitter, H.; Sariciftci, N. S. Low-Threshold Blue Lasing in Epitaxially Grown Para-Sexiphenyl Nanofibers. *J. Lumin.* **2005**, *112*, 321−324.

(22) Balzer, F.; Pogantsch, A.; Rubahn, H. G. Temperature Dependent Analysis of Three Classes of Fluorescence Spectra from P-6P Nanofiber Films. *J. Lumin.* **2009**, *129*, 784−789.

(23) Balzer, F.; Bordo, V.; Simonsen, A.; Rubahn, H.-G. Optical Waveguiding in Individual Nanometer-Scale Organic Fibers. *Phys. Rev. B: Condens. Matter Mater. Phys.* **2003**, *67*, 115408(1−8).

(24) Leißner, T.; Thilsing-Hansen, K.; Lemke, C.; Jauernik, S.; Kjelstrup-Hansen, J.; Bauer, M.; Rubahn, H.-G. Surface Plasmon Polariton Emission Prompted by Organic Nanofibers on Thin Gold Films. *Plasmonics* **2011**, *7*, 253−260.

(25) Quochi, F.; Cordella, F.; Mura, A.; Bongiovanni, G.; Balzer, F.; Rubahn, H. G. Gain Amplification and Lasing Properties of Individual Organic Nanofibers. *Appl. Phys. Lett.* **2006**, *88*, 041106(1−3).

(26) Quochi, F.; Saba, M.; Cordelia, F.; Gocalinska, A.; Corpino, R.; Marceddu, M.; Anedda, A.; Andreev, A.; Sitter, H.; Sariciftci, N. S.; et al. Temperature Tuning of Nonlinear Exciton Processes in Self-Assembled Oligophenyl Nanofibers under Laser Action. *Adv. Mater. (Weinheim, Ger.)* **2008**, *20*, 3017−3021.

(27) Camposeo, A.; Di Benedetto, F.; Cingolani, R.; Pisignano, D. Full Color Control and White Emission from Conjugated Polymer Nanofibers. *Appl. Phys. Lett.* **2009**, *94*, 043109(1−3).

(28) Yang, Y.; Turnbull, G. A.; Samuel, I. D. W. Hybrid Optoelectronics: A Polymer Laser Pumped by a Nitride Light-Emitting Diode. *Appl. Phys. Lett.* **2008**, *92*, 163306(1−3).

(29) Zhao, Y.; Truhlar, D. G. The M06 Suite of Density Functionals for Main Group Thermochemistry, Thermochemical Kinetics, Non-covalent Interactions, Excited States, and Transition Elements: Two New Functionals and Systematic Testing of Four M06-Class Functionals and 12 Other Functionals. *Theor. Chem. Acc.* **2008**, *120*, 215−241.

(30) Zhao, Y.; Truhlar, D. G. The M06 Suite of Density Functionals for Main Group Thermochemistry, Thermochemical Kinetics, Non-covalent Interactions, Excited States, and Transition Elements: Two New Functionals and Systematic Testing of Four M06-Class

Functionals and 12 Other Functionals. *Theor. Chem. Acc.* **2008**, *119*, 525.

(31) Lumpi, D.; Horkel, E.; Plasser, F.; Lischka, H.; Fröhlich, J. Synthesis, Spectroscopy, and Computational Analysis of Photoluminescent Bis(aminophenyl)-Substituted Thiophene Derivatives. *ChemPhysChem* **2013**, *14*, 1016−1024.

(32) Charaf-Eddin, A.; Planchat, A.; Mennucci, B.; Adamo, C.; Jacquemin, D. Choosing a Functional for Computing Absorption and Fluorescence Band Shapes with TD-DFT. *J. Chem. Theory Comput.* **2013**, *9*, 2749−2760.

(33) Jacquemin, D.; Planchat, A.; Adamo, C.; Mennucci, B. TD-DFT Assessment of Functionals for Optical 0−0 Transitions in Solvated Dyes. *J. Chem. Theory Comput.* **2012**, *8*, 2359−2372.

(34) da Silva Filho, D. A.; Friedlein, R.; Coropceanu, V.; Ohrwall, G.; Osikowicz, W.; Suess, C.; Sorensen, S. L.; Svensson, S.; Salaneck, W. R.; Brédas, J.-L. Vibronic Coupling in the Ground and Excited States of the Naphthalene Cation. *Chem. Commun. (Cambridge, U.K.)* **2004**, 1702−1703.

(35) Frisch M. J.; Trucks, G. W.; Schlegel, H. B.; Scuseria, G. E.; Robb, M. A.; Cheeseman, J. R.; Scalmani, G.; Barone, V.; Mennucci, B.; Petersson, G. A.; et al. *Gaussian 09*, revision A.02; Gaussian, Inc.: Wallingford, CT,2009.

(36) Greenham, N. C.; Samuel, I. D. W.; Hayes, G. R.; Phillips, R. T.; Kessener, Y. A. R. R.; Moratti, S. C.; Holmes, A. B.; Friend, R. H. Measurement of Absolute Photoluminescence Quantum Efficiencies in Conjugated Polymers. *Chem. Phys. Lett.* **1995**, *241*, 89−96.

(37) Horowitz, G.; Kouki, F.; El Kassmi, A.; Valat, P.; Wintgens, V.; Garnier, F. Structure-Dependent Fluorescence in Sexithiophene Single Crystals. *Adv. Mater. (Weinheim, Ger.)* **1999**, *11*, 234−238.

(38) Loi, M. A.; da Como, E.; Dinelli, F.; Murgia, M.; Zamboni, R.; Biscarini, F.; Muccini, M. Supramolecular Organization in Ultra-Thin Films of α-Sexithiophene on Silicon Dioxide. *Nat. Mater.* **2004**, *4*, 81−85.

(39) Da Como, E.; Loi, M. A.; Murgia, M.; Zamboni, R.; Muccini, M. J-Aggregation in α-Sexithiophene Submonolayer Films on Silicon Dioxide. *J. Am. Chem. Soc.* **2006**, *128*, 4277−4281.

(40) Piaggi, A.; Lanzani, G.; Bongiovanni, G.; Loi, M. A.; Mura, A.; Graupner, W.; Meghdadi, F.; Leising, G. Optical Properties of Polycrystalline Films. *Opt. Mater. (Amsterdam, Neth.)* **1998**, *9*, 489−493.

(41) Piaggi, A.; Lanzani, G.; Bongiovanni, G.; Mura, A.; Graupner, W.; Meghdadi, F.; Leising, G.; Nisoli, M. Emission Properties of Para-Hexaphenyl Polycrystalline Films. *Phys. Rev. B: Condens. Matter Mater. Phys.* **1997**, *56*, 10133−10137.

(42) Baker, K. N.; Fratini, A. V.; Resch, T.; Knachel, H. C.; Adams, W. W.; Socci, E. P.; Farmer, B. L. Crystal Structures, Phase Transitions and Energy Calculations of Poly(p-Phenylene) Oligomers. *Polymer* **1993**, *34*, 1571−1587.

(43) Horowitz, G.; Bachet, B.; Yassar, A.; Lang, P.; Demanze, F.; Fave, J.; Garnier, F. Growth and Characterization of Sexithiophene Single Crystals. *Chem. Mater.* **1995**, *7*, 1337−1341.

(44) Casado, J.; Hernández, V.; López Navarrete, J. T.; Algarra, M.; da Silva Filho, D. A.; Yamaguchi, S.; Rondão, R.; Seixas de Melo, J. S.; Navarro-Fuster, V.; Boj, P. G.; et al. Amplified Spontaneous Emission in Pentathienoacene Dioxides by Direct Optical Pump and by Energy Transfer: Correlation with Photophysical Parameters. *Adv. Opt. Mater.* **2013**, *1*, 588−599.

(45) Casado, J.; Zgierski, M. Z.; Ewbank, P. C.; Burand, M. W.; Janzen, D. E.; Mann, K. R.; Pappenfus, T. M.; Berlin, A.; Pérez-Inestrosa, E.; Ortiz, R. P.; et al. Exploration of Ground and Excited Electronic States of Aromatic and Quinoid S,S-Dioxide Terthiophenes. Complementary Systems for Enhanced Electronic Organic Materials. *J. Am. Chem. Soc.* **2006**, *128*, 10134−10144.

(46) Filho, D. A. da S.; Coropceanu, V.; Fichou, D.; Gruhn, N. E.; Bill, T. G.; Gierschner, J.; Cornil, J.; Brédas, J.-L. Hole-Vibronic Coupling in Oligothiophenes: Impact of Backbone Torsional Flexibility on Relaxation Energies. *Philos. Trans. R. Soc., A* **2007**, *365*, 1435−1452.

(47) Millar, D. P.; Robbins, R. J.; Zewail, A. H. Picosecond Dynamics of Electronic Energy Transfer in Condensed Phases. *J. Chem. Phys.* **1981**, *75*, 3649−3659.

(48) Pansu, R. B.; Yoshihara, K.; Arai, T.; Tokumaru, K. Convolution Analysis of the Pyrene Excimer Formation in Membranes. *J. Phys. Chem.* **1993**, *97*, 1125−1133.

(49) Note that Equation 5 assumes a single exponential decay. In fact, τ_{NR} represents the p6P nonradiative decay time constant in donor material regions involved in diffusion-assisted RET, whereas donor regions very close to donor/acceptor interfaces, where RET is a direct and ultrafast process yielding a much shorter τ_{NR} value, give a negligible contribution to the equation.

(50) Wen, X.; Yu, P.; Yuan, C. T.; Ma, X.; Tang, J. Singlet and Triplet Carrier Dynamics in Rubrene Single Crystal. *J. Phys. Chem. C* **2013**, *117*, 17741−17747.

(51) Platt, A. D.; Kendrick, M. J.; Loth, M.; Anthony, J. E.; Ostroverkhova, O. Temperature Dependence of Exciton and Charge Carrier Dynamics in Organic Thin Films. *Phys. Rev. B: Condens. Matter Mater. Phys.* **2011**, *84*, 235209(1−16).